Large-scale Synthesis of Urchin-like Mesoporous TiO_2 Hollow Spheres by Targeted Etching and Their Photoelectrochemical Properties

Jia Hong Pan, Xing Zhu Wang, Qizhao Huang, Chao Shen, Zhen Yu Koh, Qing Wang, Astrid Engel, and Detlef W. Bahnemann*

A versatile targeted etching strategy is developed for the large-scale synthesis of urchin-like mesoporous TiO_2 hollow spheres (UMTHS) with tunable particle size. Its key feature is the use of a low-temperature hydrothermal reaction of surface-fluorinated, amorphous, hydrous TiO_2 solid spheres (AHTSS) under the protection of a polyvinylpyrrolidone (PVP) coating. With the confinement of PVP and water penetration, the highly porous AHTSS are selectively etched and hollowed by fluoride without destroying their spherical morphology. Meanwhile TiO_2 hydrates are gradually crystallized and their growth is preferentially along anatase (101) planes, reconstructing an urchin-like shell consisting of numerous radially arranged single-crystal anatase nanothorns. Complex hollow structures, such as core–shell and yolk–shell structures, can also be easily synthesized via additional protection of the interior by prefilling AHTSS with polyethylene glycol (PEG). The hollowing transformation is elucidated by the synergetic effect of etching, PVP coating, low hydrothermal reaction temperature, and the unique microstructure of AHTSS. The synthesized UMTHS with a large surface area of up to 128.6 $m^2 g^{-1}$ show excellent light-harvesting properties and present superior performances in photocatalytic removal of gaseous nitric oxide (NO) and photoelectrochemical solar energy conversion as photoanodes for dye-sensitized mesoscopic solar cells.

1. Introduction

Efficient solar energy harvesting calls for advanced semiconducting materials as the key building block. Research over the past few decades has demonstrated that a variety of semiconductors is capable of utilizing sunlight to produce electrical and chemical energy.[1,2] As an important transition-metal oxide semiconductor, titanium dioxide (TiO_2) has attracted numerous interests in view of its outstanding physicochemical properties, such as suitable band position, non-toxicity, low cost, chemical and photonic stability, and biocompatibility. Photoelectrochemical conversions mediated by TiO_2 have led to an array of important applications including environmental photocatalysis, solar fuels production, and dye-sensitized solar cells (DSCs).[2–6] Optimizing the structural properties of TiO_2 is essential to boost its performances. Thus, various synthetic strategies have been developed to control over the crystal structure, surface area, porosity, and morphology of TiO_2.[7–11] The most prominent example is TiO_2 hollow spheres, which have presented a substantial cutting edge innovation for solar energy conversion owing to their low density, 3D hierarchical structure, large surface area, monodisperse nature easy for integrating into devices, superior light scattering and reflection properties, excellent loading capacity, etc.[4,12–16]

Considerable efforts have been devoted to the synthesis of TiO_2 hollow spheres. Traditional template route using polymer, carbon or SiO_2 spheres as hard templates has been well established to produce TiO_2 hollow spheres.[8,17,18] Recent development has been steered to template-free route, and one-pot hydro/solvothermal approach has emerged to be a convenient and cost-effective synthetic method. Under the critical conditions, TiO_2 precursors undergo multiple transitions in crystallography, microstructure and morphology to form hollow spheres. The as-crystallized TiO_2 nanobuilding blocks (NBBs) can spontaneously assemble to a thermodynamically favored spherical structure, followed with phase transformation and generation of hollow interior based on a dissolution–recrystallization mechanism typically induced by corrosive agents, such as H_2O_2[14] and fluorides.[15,19–21] Kinetic controls of these indiscriminate transitions are difficult, which, indeed, is the main reason that controllable and predictable synthesis of TiO_2 hollow spheres by hydro/solvothermal methods have not been achieved up to now. Diluted media are routinely employed nowadays in hydro/solvothermal methods to ease their synthesis,

Dr. J. H. Pan, Dr. X. Z. Wang, Q. Huang, C. Shen, Z. Y. Koh, Prof. Q. Wang
Department of Materials Science and Engineering
Faculty of Engineering
NUSNNI-NanoCore
National University of Singapore
5 Engineering Drive 2, Singapore, 117576, Singapore
E-mail: msewq@nus.edu.sg
Dr. J. H. Pan, A. Engel, Prof. D. W. Bahnemann
Photocatalysis and Nanotechnology Group
Institut für Technische Chemie
Gottfried Wilhelm Leibniz Universität Hannover
Callinstraβe 3, D-30167, Hannover, Germany

DOI: 10.1002/adfm.201300946

which inevitably lead to extremely low yields of about dozens of micrograms per synthesis.[8,22,23] Moreover, synthesis of TiO_2 hollow spheres with porous structure and large surface area remains a challenge. The NBBs are prone to form closely packed spherical assembly, in contrast to the formation of porous and hollow structure. To promote the formation of hollow structure, rapid crystal growth along with chemical dissolution process is vigorously triggered. As a result, specific surface area is largely sacrificed. Hence it is not surprising that the mostly investigated TiO_2 hollow spheres prepared from hydrothermal reactions of TiF_4 in weakly acidic solutions have a poorly porous structure with limited surface areas of 20–60 $m^2\ g^{-1}$.[23–27]

In an effort to synthesize porous TiO_2 hollow spheres with a large surface area, we consider placing the formation of spherical TiO_2 and the hollowing process at two separate synthetic stages to facilitate the morphological control, as perfectly demonstrated for SiO_2 hollow spheres recently.[28–30] However, different from amorphous SiO_2, controlling the phase transition and crystal growth in TiO_2 becomes more critical so that the hollow structures are not affected. Therefore, TiO_2 NBBs should be carefully incubated in the mother spherical structure during the hollowing process not only to maintain the spherical structure, but also to deliver a large surface area. Based on these considerations, we develop a novel strategy for the large–scale (in gram quantities) synthesis of uniform urchin-like mesoporous TiO_2 hollow spheres (UMTHS) consisting of 1D single crystal anatase nanothorns with exposed {101} facets. This method involves targeted etching of self-organized amorphous hydrous TiO_2 solid spheres (AHTSS) (**Scheme 1**). The UMTHS are grown from the spontaneous reconstruction of surface–fluorinated AHTSS in the presence of surface coating of polyvinylpyrrolidone (PVP) under mild hydrothermal conditions. Adjusting the experimental parameters leads to the controllable synthesis of UMTHS with tunable sphere size and diverse interiors varying from solid, hollow, core-shell and yolk-shell structures. The synthesized UMTHS have a large surface area up to 128.6 $m^2\ g^{-1}$ and show excellent performances in environmental photocatalysis and DSCs.

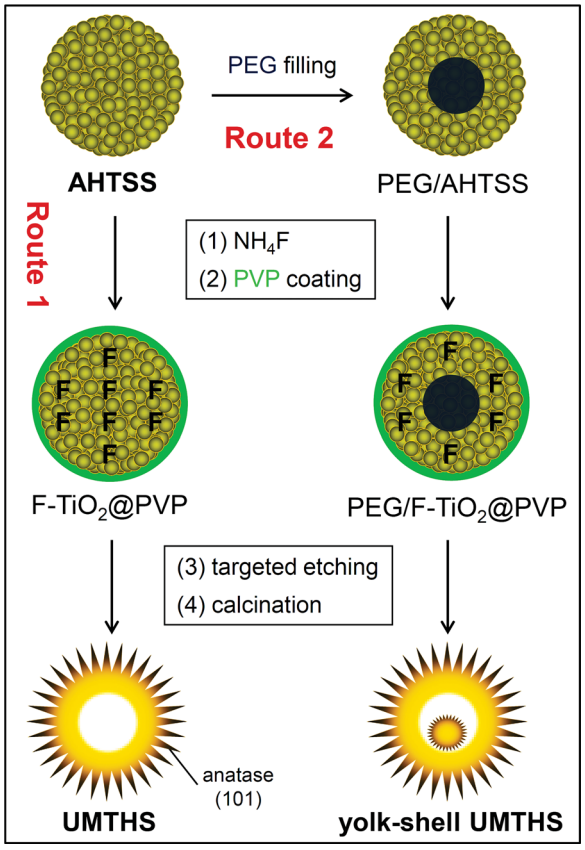

Scheme 1. Hollowing transformation from amorphous hydrous TiO_2 solid spheres (AHTSS) to urchin-like mesoporous TiO_2 hollow spheres (UMTHS) (Route 1) and their yolk–shell derivatives (Route 2) via a targeted etching process.

2. Results and Discussion

2.1. Targeted Etching Reconstruction of AHTSS to UMTHS

Our synthesis started from the preparation of AHTSS by direct precipitation of titanium isopropoxide ($Ti(O\text{-}iPr)_4$, TTIP) in a mixed ethanol–acetonitrile solution with small amounts of H_2O and NH_3, where NH_3 acts as an agglomeration prompter and morphological controller to direct the self-organization of primary $Ti(O\text{-}iPr)_x(OH)_{4-x}$ hydrates to form uniform spherical agglomerates.[31] The force that drives the assembly of TiO_2 hydrates is believed to be hydrogen bonding enhanced by NH_3. By tuning the molar ratio of H_2O to TTIP (R_H) from 15 to 2.5, monodispersed AHTSS with controllable sizes (0.3–1.0 μm) can be feasibly prepared (see Figure S1 in Supporting Information). We take AHTSS derived from $R_H = 5$ as an example for the subsequent synthesis of UMTHS unless otherwise stated.

The morphology and microstructure of AHTSS are shown in **Figure 1**. As identified by scanning electron microscopy (SEM) and transmission electron microscopy (TEM), AHTSS are solid spheres with a uniform diameter of ~490 nm. A close observation to the surface by TEM in Figure 1d revealed that each sphere consists of plentiful nanosized amorphous TiO_2 hydrates, amongst which numerous voids are formed. As revealed by N_2 sorption analysis (**Figure 2**), AHTSS exhibit type-IV isotherm plots with an H1 hysteresis loop, the characteristic of uniform mesopores formed by closely packed nanoparticles. The specific surface area is as high as 328.6 $m^2\ g^{-1}$ and the average pore size is 3.4 nm.

The surface of nanosized TiO_2 hydrates in AHTSS is largely terminated with hydroxyl groups, while the organic ligands, e.g. –*i*Pr, are largely removed after a thorough hydrolysis. As demonstrated by the thermogravimetric analysis (TGA), AHTSS exhibit a slight weight loss (<13%) at temperature lower than 300 °C (Figure S2), which can be attributed to the dehydration of hydrous TiO_2. The hydrophilic nature of AHTSS is beneficial to their chemical bonding with the foreign species including F^- and PVP molecules.

By simply mixing the as-prepared AHTSS with fluoride at an F/Ti molar ratio (R_F) of 0.12, the surface of AHTSS could be fluorinated through ligand exchange between surface hydroxyl

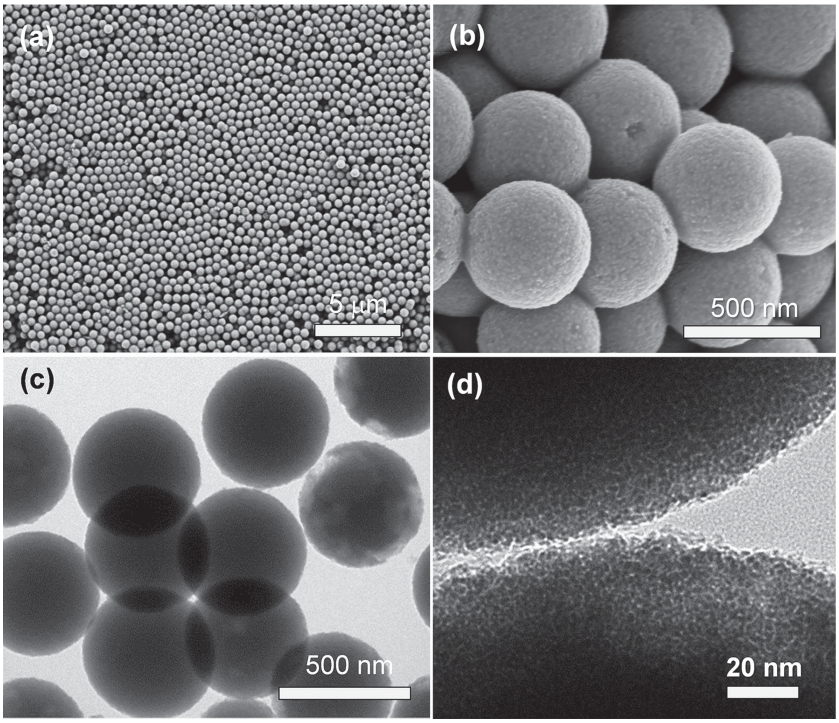

Figure 1. SEM (a,b) and TEM (c,d) images of monodispersed AHTSS consisting of numerous nanosized TiO_2 hydrates.

groups and F^-, resulting in a distinct increase in solution's pH value. Typically, when NH_4F was introduced, the pH value of the suspension solution was increased from 5.5 to 8.5 even although NH_4F itself shows acidic properties. Subsequently, PVP was introduced into the suspension. AHTSS were readily coated by PVP through the hydrogen bonding between the carbonyl groups of PVP and the hydroxyls on AHTSS surface, forming an F–TiO_2@PVP core–shell structure (see Route 1 of Scheme 1). As revealed by SEM analysis (Figure S3a), F–TiO_2@PVP retains spherical morphology, and its surface is smoother than AHTSS. TEM analysis further demonstrates that a thin PVP layer with a thickness of 5–15 nm is formed on the surface of TiO_2 (Figure S3b). These microscopical observations are consistent with the results obtained from the infrared spectroscopy in PVP-coated SiO_2 spheres by Yin and coworkers,[28,32] who further proved that the formed PVP porous coating has excellent chemical stability at elevated temperature.

Targeted etching process was conducted by treating the formed F–TiO_2@PVP aqueous suspension hydrothermally at a mild temperature of 110 °C for 4 h. UMTHS were finally obtained by calcining the powder after hydrothermal reaction. **Figure 3**a and S4 shows their representative SEM micrographs with different magnifications. UMTHS are nearly monodisperse with uniform particle size around 450 nm. The shells were composed of radially standing 1D nanothorns, assembling an urchin-like hierarchical structure. Their hollow interior is clearly revealed with some broken spheres (Figure S4), and can be further confirmed by TEM analysis, as shown in Figure 3b,c. The spherical shell consisting of radial nanothorns has a thickness of 70–100 nm, in good agreement with the SEM results. It is noteworthy that the single hollow sphere is polycrystalline due to radial orientation of nanothorns, as revealed by selected-area electron diffraction (inset of Figure 3d). However, each nanothorn, with a uniform diameter of 10–20 nm and a length of 40–60 nm presents a single-crystal nature and possesses the lattice fringes of anatase (101) plane with a *d*-spacing of 0.35 nm aligned over the single nanothorn, according to the high-resolution TEM analysis (Figure 3e).

Unlike AHTSS, the N_2 sorption isotherms of UMTHS show a steep H2 loop (Figure 2a). Their BET surface area is 128.6 $m^2 g^{-1}$. The capillary condensation steps shift to higher relative pressures of 0.6–1.0, which is closely related to the increase in pore size. As shown in Figure 2b, UMTHS show a broad pore size distribution in meso- to near-macroporous regions, which are associated with the mesopores among nanothorns and the large voids from the hollow interiors, respectively. The average pore size is calculated to be 12.5 nm.

2.2. Formation Mechanism of Hollow and Urchin-like Superstructure

Our repeated experiments have verified that the present targeted-etching process is highly reproducible and scalable. It gave a yield over 95% with negligibly isolated or ill-defined particles in the final products. Hydrothermal re-treatment of the supernatant with NaOH did not obtain any solid product, indicating PVP coating on the AHTSS surface truly stabilizes the spherical structure and, more importantly, restrains the diffusion of the dissolved Ti species out of the mother sphere. As a result, under the confinement of PVP while the adsorbed fluorides are constrained to only etch the parent sphere, the dissolved Ti species are prone to re-deposit and crystallize within the sphere to form a well-defined hierarchical structure. In the absence of PVP coating, hydrothermal treatment of AHTSS with fluoride merely leads to the formation of a mixture of free nanoparticles and distorted spheres, as shown in Figure S5.

By separating sphere formation and hollowing process, each sphere is crystallized and hollowed independently inside the PVP coating. Therefore, the conventional factors such as concentration that is able to interfere with the formation of hollow spheres can be successfully overcome. As such, the reaction can be conducted at a high concentration, which remarkably improves the production of TiO_2 up to the gram scale, currently the largest to the best of our knowledge.

With the protection of PVP, water is used as the sole reaction medium in our synthetic protocol. In contrast to the combined sol-gel and solvothermal method with which mesoporous TiO_2 solid spheres are synthesized in ethanol-rich media at 160–220 °C,[7,11,33–35] the higher polarity of water facilitates the crystallization of TiO_2 at a relatively low temperature of 110 °C. The significant decrease in reaction temperature and system pressure is beneficial to preserve the morphology of hollow sphere and to control the crystal growth of anatase TiO_2.

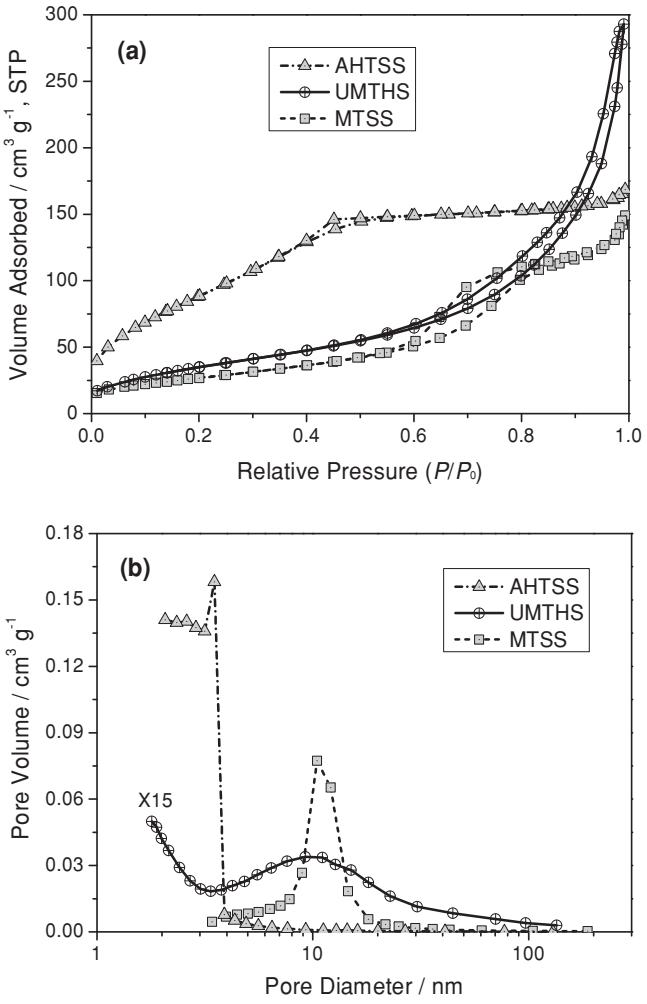

Figure 2. N_2 sorption isotherms (a) and pore size distributions (b) of AHTSS, UMTHS, and mesoporous TiO_2 solid spheres (MTSS).

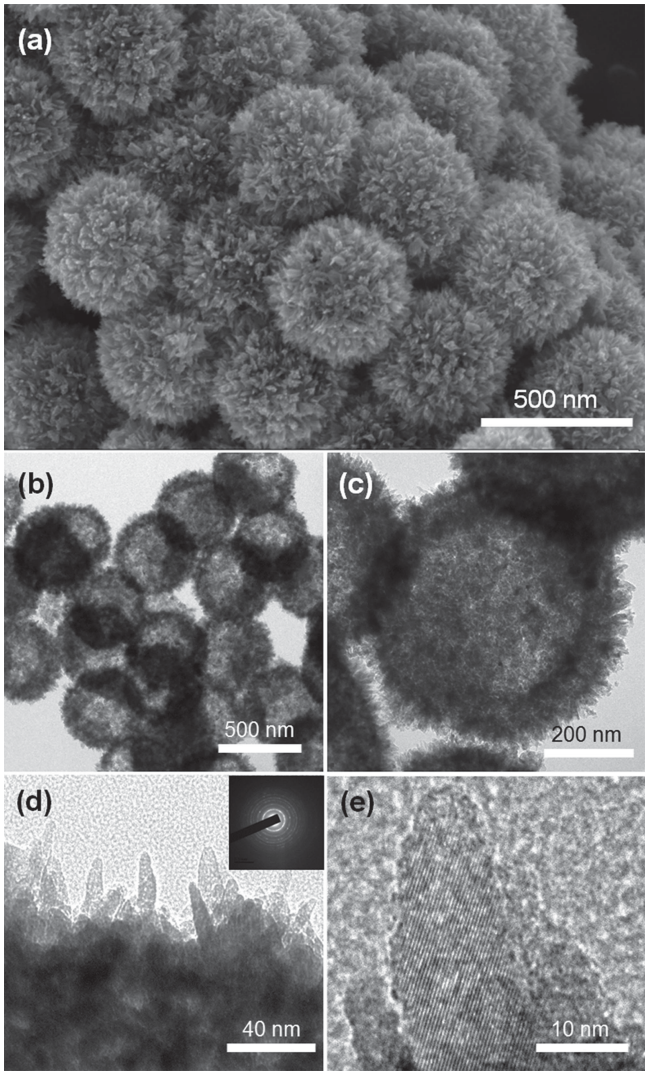

Figure 3. SEM (a) and TEM (b-e) micrographs of UMTHS consisting of radially arranged anatase nanothorns with exposed {101} facets.

The presence of fluoride is essential to the formation of hollow structure and urchin-like shell. Control experiments using different dosages of fluoride reveal its dual functions in hollowing and crystallization of AHTSS. **Figure 4**a shows the wide-angle X-ray diffraction (XRD) patterns of TiO_2 products obtained with different R_F of 0.08, 0.12, and 0.16. All the samples display a pure anatase phase (ICDD Card No. 21-1272). The diffraction peak of (101) plane at 25.26° is gradually sharper and more intensive with the increase of R_F, indicating enhanced crystal growth induced by fluoride, a well-known mineralizing agent. Under hydrothermal conditions, fluoride can bridge the edge-sharing polycondensation of TiO_6 octahedra, by which AHTSS dehydrate stepwise and transform to anatase phase with preferential growth along (101) plane.[19,36]

Additional to the gradual change in crystal phase, a clear morphological evolution from solid to hollow spheres, and to the isolated nanothorns disassembled from hollow spheres can be observed with the increase of R_F. As revealed in Figure 4b and 4c, mesoporous TiO_2 solid spheres (MTSS) consisting of closely packed nanocrystalline grains can be obtained at a low R_F of 0.08. Possessing a specific surface area of 107.5 m^2 g^{-1}, MTSS show similar type-IV N_2 sorption isotherms (Figure 2a) with a H1 hysteresis loop as AHTSS, implying that the mild etching process have little impact to the original packing in the mother AHTSS. Moreover, their crystal size remains uniform after etching, leading to a much narrower pore size distribution and a smaller average pore size of 10.2 nm than those of UMTHS (Figure 2b).

Increasing R_F to 0.12 enhances the etching process, creating a hollow structure in UMTHS. Meanwhile TiO_2 NBBs evolve into nanothorns due to the preferential crystal growth guided by fluoride. However, further increasing R_F to 0.16 results in the intense etching process and the formation of over-grown nanothorns. Therefore, under the increased structural stress only a few hollow spheres persist (Figure 4d), while mostly are distorted and collapsed into isolated debris of long nanothorns, as revealed by a low-magnification SEM image in Figure S6.

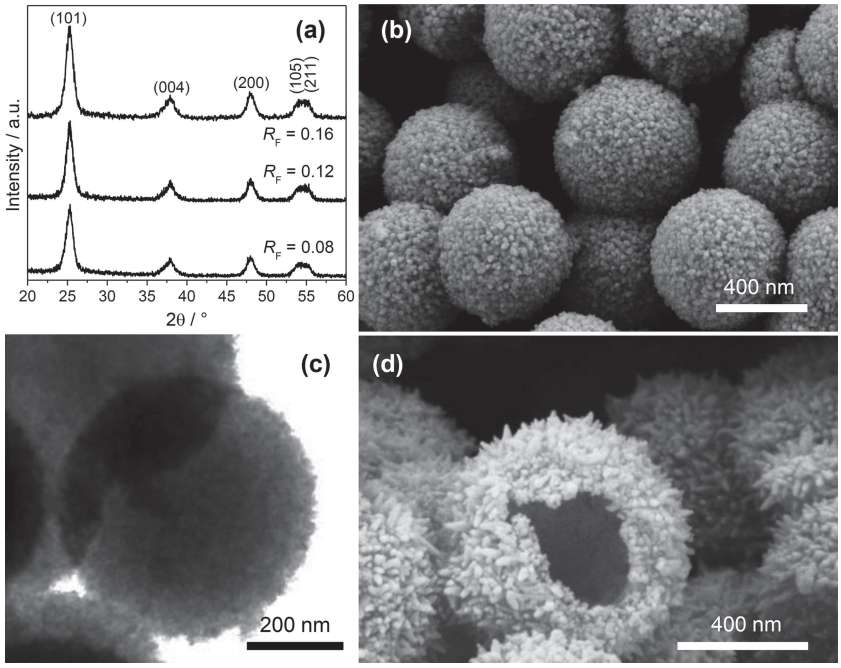

Figure 4. XRD patterns (a) of various TiO_2 spheres synthesized at different F/Ti molar rations (R_F). SEM (b) and TEM (c) images of MTSS synthesized at a R_F of 0.08. SEM image (d) of distorted TiO_2 hollow spheres synthesized at a R_F of 0.16.

To further verify our speculation and to have an insightful understanding of the targeted etching process, we monitored the continuous structural evolution during the hydrothermal reaction and with an optimal R_F of 0.12. As the TEM images shown in **Figure 5**, with the increase of reaction time AHTSS gradually turn transparent and finally transfer to hollow spheres with dense single-crystal anatase nanothorns in the shell. Crystallization and growth of nanothorns firstly occur on the surface of solid spheres with the penetration of water. A few upstanding nanothorns with anatase phase have already there after 1 h hydrothermal reaction, as clearly revealed by the high-resolution TEM image (Figure S7). This result also proves that water along with fluoride significantly facilitates the crystallization of TiO_2 even at a low hydrothermal temperature. As time elapses, anatase nanothorns gradually preside over the surface of spheres; on the other hand, the interiors of spheres become observably transparent. With the progressive pervasion of water, big voids start to appear inside the sphere with some of them in part becoming hollow after 3 h reaction, suggesting that the hollowing process occur preferentially in the interior presumably accompanied with the outward diffusion of Ti species. As a result, they will finally deposit on the inner surface of the shell to support the radial nanothorns on the outer surface. This targeted etching towards the inner spheres seems to accelerate with the reaction time: from 3 h to 3.5 h the sphere turned hollow almost entirely, indicating that the hollowing process is indeed due to the spatial divergence in the structure of AHTSS. Extending the reaction to 4 h further improves the outward diffusion of Ti species, and most of the spheres become completely hollowed.

The structural properties of AHTSS were found to be critical to the targeted etching and outward diffusion. Our AHTSS prepared with NH_3 hold several structural characteristics that are favorable for the hollowing process. Firstly, their hydrophilic surface with rich hydroxide groups not only facilitates the ion exchange with F^-, but also firms the chemical bonding with PVP coating. Secondly, their highly porous structure is beneficial for the uniform distribution of F^- throughout the spheres, and, more importantly, provides capacious space for the creation of hollow interiors following the outward diffusion. Thirdly, the tiny primary TiO_2 hydrates assembled in the spheres through weak hydrogen bonding show high mobility for dissolution and outward Ostwald ripening under the hydrothermal condition. Fourthly, the self-organized AHTSS show an interesting spatial divergence in structure throughout the sphere: the primary TiO_2 hydrates located in the core are relatively smaller and more densely packed, thereby having a higher mean curvature and surface energy, compared with those close to the surface.[20,24,29] They present relatively high reactivity and mobility towards etching and reconstruction. During hydrothermal process, outward diffusion can be readily initiated from their spherical interiors. Indeed, AHTSS can also be prepared according to previous reports using other morphological

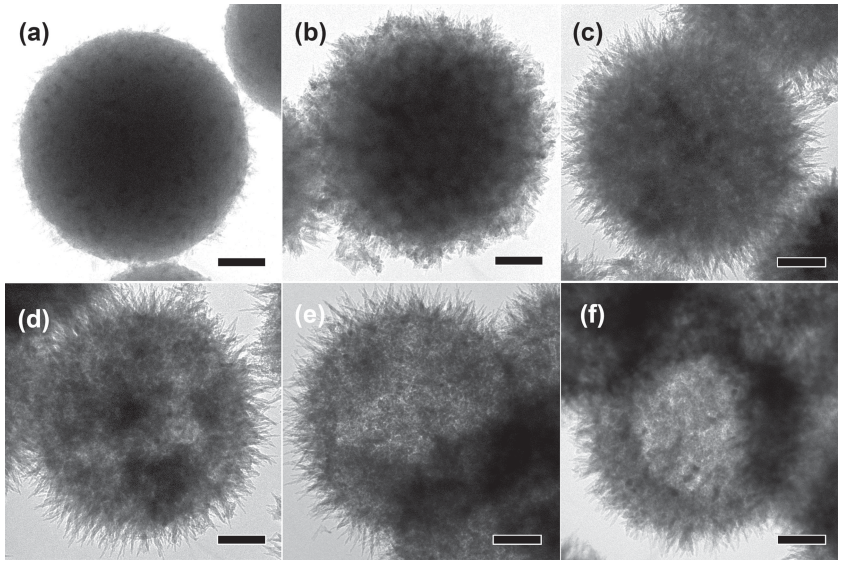

Figure 5. TEM images showing the hollowing transition of AHTSS during targeted etching for different time: 1 (a), 2 (b), 3 (c, d), 3.5 (e), 4 (f) h. All the scale bars are 100 nm.

controllers, such as dodecylamine (DDA) surfactant[37] and NaCl;[38,39] however, the resultant AHTSS could not be hollowed based on our control experiments. Presumably it is a result of the relatively small accessible surface area to the etching agent and the large attraction forces between hydrous TiO_2 NBBs due to their robust hybridization with surfactant molecules or the strong electrostatic interactions induced by NaCl.[40]

Based on the above observations, the formation mechanism of UMTHS can be elucidated as a synergetic effect of unique microstructures of AHTSS, low dosage of fluoride, PVP coating, water-based solvent, and a mild hydrothermal temperature as low as 110 °C. In contrast to the one-pot or self-template solvothermal methods conducted at 160–200 °C,[23,27,37] the low-temperature hydrothermal reaction with the assistances of fluoride and PVP coating allows the controllable transformation of highly porous AHTSS with appropriate textural properties to UMTHS with a hollow interior and abundant anatase nanothorns with exposed {101} facets radially arranged on the shell. It is noteworthy that our targeted etching process mediated by the fluoride within the mother spheres greatly reduces its dosage to a level ($R_F = 0.12$) greatly lower than ever reported so far,[19] which significantly prevents TiO_2 NBBs from crystal fusion and in turn helps to direct the preferential growth of anatase along (101) plane, and eventually renders a hierarchical and hollow structure with a large surface area.

2.3. Towards Size and Hollow-Structure Controllable Synthesis

Tuning the size of spheres is of great importance for various applications.[7,34] The targeted etching route elegantly decouples the hollowing process from sphere formation process, providing great flexibility for the size-controllable synthesis of UMTHS by using different-size AHTSS. **Figure 6** shows UMTHS with uniform diameters of ca. 630, 390, and 280 nm. All the hollow spheres possessed similar urchin-like shell and hollow interiors. Notably, the hollow structure of 280 nm-sized UMTHS is not as uniform as others. Presumably, the spatial divergence of nanosized TiO_2 hydrates diminishes in the small AHTSS. Consequently, the etching process loses its preference towards the inner core.

Moreover, the targeted etching method has great versatility for hollow structure engineering. The high porosity and large surface area of AHTSS provide an excellent platform to construct complex hollow structures. For instance, polyethylene glycol (PEG) can be filled into the inner space of AHTSS prior to fluoride adsorption and PVP coating (see Route 2 of Scheme 1). The presence of PEG in the sphere core hinders the penetration of fluoride and water upon soaking in fluoride solution, and hence the subsequent etching towards the core of AHTSS during hydrothermal process. With the subsequent PVP coating on the outer surface, targeted etching is confined within the space non-protected. That is, during hydrothermal process the TiO_2 species located between the interior PEG and exterior PVP were selectively etched, creating a sphere-in-sphere structure. More interestingly, simply tuning the reaction time may lead to a structural transformation from core-shell to yolk-shell structure.

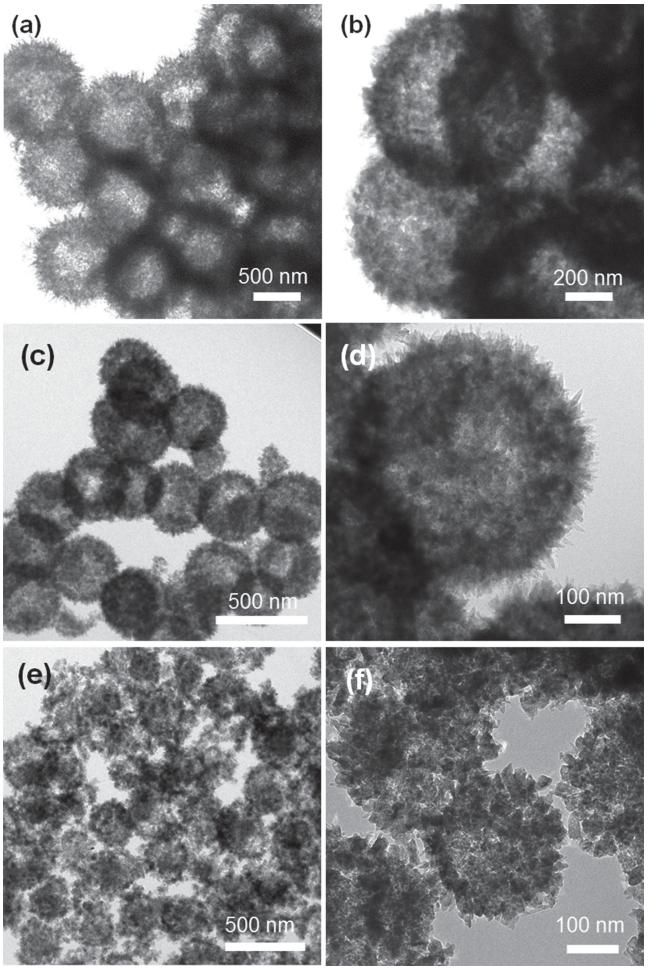

Figure 6. TEM images of UMTHS with different sizes of 630 (a,b), 370 (c,d), and 240 nm (e,f).

As shown in **Figure 7**a and b, a solid sphere centers inside the mother sphere after 2-h hydrothermal reaction, building up a core–shell-like structure. The solid sphere in the core is supported by anatase nanocrystallites that have not been etched completely. Upon further extending the reaction time to 3 h, the core spheres are settled down and separated from the outer spheres, creating a yolk–shell structure (Figure 7c,d). The resultant yolk-shell spheres possessed similar urchin-like shells as that of UMTHS. However, their shell thickness of 40–70 nm was relatively smaller, which may be due to the Ti species in inner spheres did not diffuse to shell and participate in the construction of urchin-like superstructure.

2.4. Environmental Photocatalysis and Dye-Sensitized Solar Cells

Owing to their large surface area, spherical morphology, hollow structure, and radial 1D nanothorns with single anatase phase, UMTHS are useful for various applications. Here we have investigated their optoelectronic properties and highlight their excellent performances in photocatalytic oxidation of gaseous nitric oxide (NO) and photoanodes for DSCs.

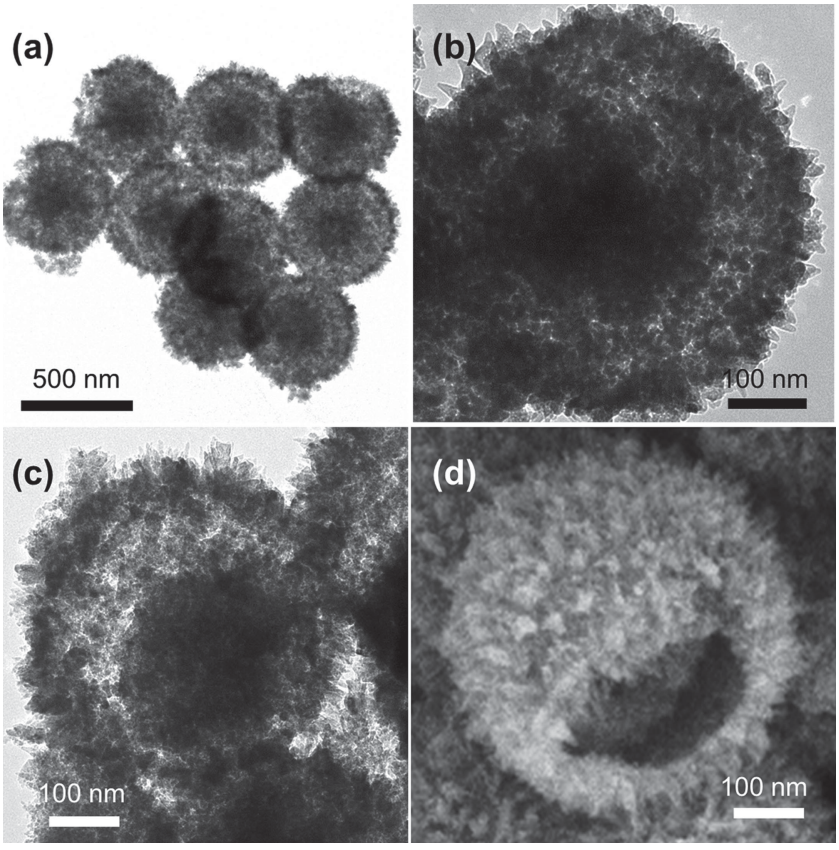

Figure 7. TEM (a-c) and SEM (d) images of UMTHS with an additional core-shell (a,b) or yolk–shell (c,d) structure synthesized by targeted etching for 2 and 3 h, respectively.

Figure 8 shows the UV-visible diffuse reflectance spectra of UMTHS and a reference TiO_2 (Aeroxide P25). Both samples show a significant increase in the absorption at wavelengths shorter than 400 nm, which can be assigned to the intrinsic band-to-band absorption of TiO_2. However, the absorption edge of UMTHS is shifted to shorter wavelength compared with P25. This could be caused by the crystal size effect of the smaller nanosized anatase crystallites in UMTHS, and the existence of an additional narrower band-gap rutile phase (~25%) in P25.[37] According to Kubelka–Munk Function, the bandgap energy (E_g) for indirect band gap semiconductors can be simply estimated from a plot of $(A/\lambda)^{1/2}$ versus $1240/\lambda$, where A is absorbance, and λ is the associated wavelength. As shown in the inset, UMTHS are estimated to have an E_g of 3.12 eV, which is slightly larger than that of P25 (E_g = 3.07 eV). Moreover, UMTHS exhibit a stronger absorption in the UV-visible range of 300–630 nm, compared with P25. Clearly, the rough spherical surface with radial nanothorns along with the hollow interior dramatically improves the light harvesting. Moreover, the steepness of the absorption band for UMTHS is higher than that for P25. This, together with an additionally excitonic peak at ca. 326 nm, indicates that TiO_2 nanocrystallites in UMTHS are much more uniform in size than nanoparticulate P25.[37]

Air pollution by NO emission from urban and industrial areas is harmful to the environment and human health. Semiconductor photocatalysis has been proven to be efficient to remove NO by photo-oxidation at ambient conditions.[6,41] Herein we assessed the photocatalytic activity of UMTHS using NO as a probe molecule. **Figure 9**a shows the time course of concentrations of the gaseous NO, the oxidation product, NO_2, and the sum of NO and NO_2, denoted as NO_x, over UMTHS and P25 under the UV(A) irradiation. Initially, an adsorption–desorption equilibrium of NO at 1ppm was reached over photocatalysts in the dark. Upon UV(A) irradiation, the concentration of NO decreased, and a simultaneous increase in NO_2 was recorded due to photocatalytic oxidation of NO to NO_2. The concentration of NO_x was less than 1 ppm due to the subsequent oxidative mineralization of NO_2 to NO_3^-. Compared with P25, UMTHS showed sharper decreases in NO and NO_x, and higher NO_2 formation. Their photonic efficiencies were calculated and depicted in Figure 9b. It can be seen that UMTHS show improved photonic efficiency in NO oxidation and much higher efficiency in total NO_x removal compared with P25. It was reported that the photocatalytic oxidation of NO to NO_2 is critically dependent on the surface area of TiO_2 since TiO_2 may be deactivated by the adsorbed NO_3^-.[41,42] Thus, the enhanced photocatalytic activity of UMTHS can be attributed to their superior structural properties: (1) enlarged specific surface areas thus providing more reaction sites for photocatalysis; (2) the hierarchical architecture allowing efficient mass transport, and permitting effective light scattering inside its interior and among the well-oriented nanothorns to enhance light harvesting for the generation of charge

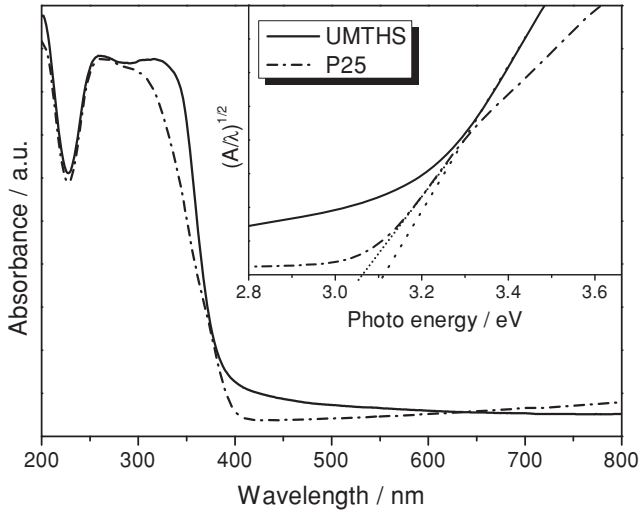

Figure 8. UV-vis absorption spectra of UMTHS and Aeroxide TiO_2 (P25) nanoparticles; The inset shows the corresponding plots of Kubelka-Munk function $(A/\lambda)^{1/2}$ versus the energy of light $(1240/\lambda)$.

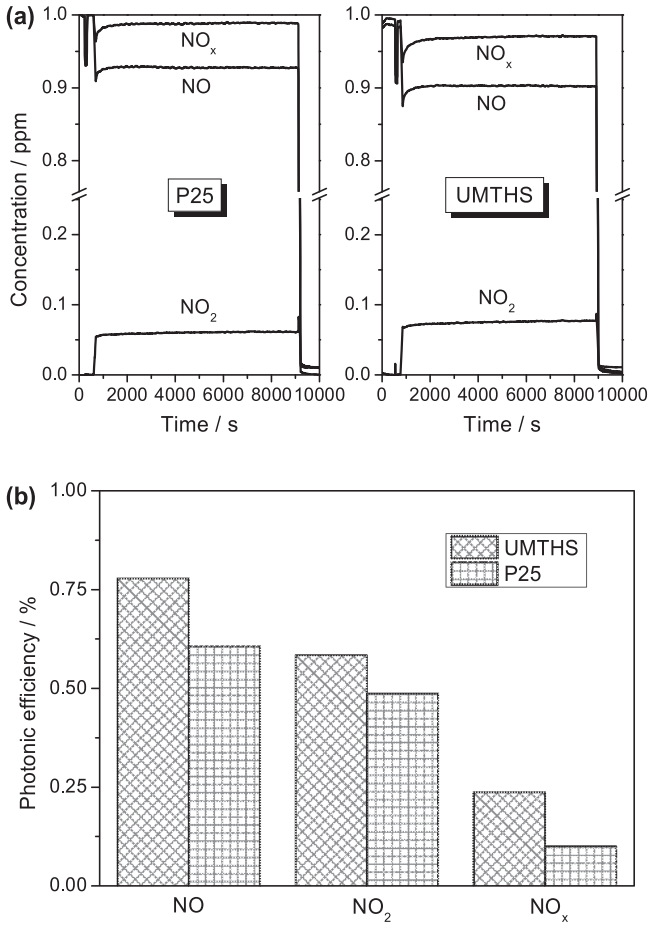

Figure 9. (a) Time course of the concentrations of gaseous NO, NO_2 and NO_x over UMTHS and P25 under the UV(A) irradiation; (b) Photonic efficiencies of UMTHS and P25 in NO oxidation, NO_2 formation and NO_x removal processes.

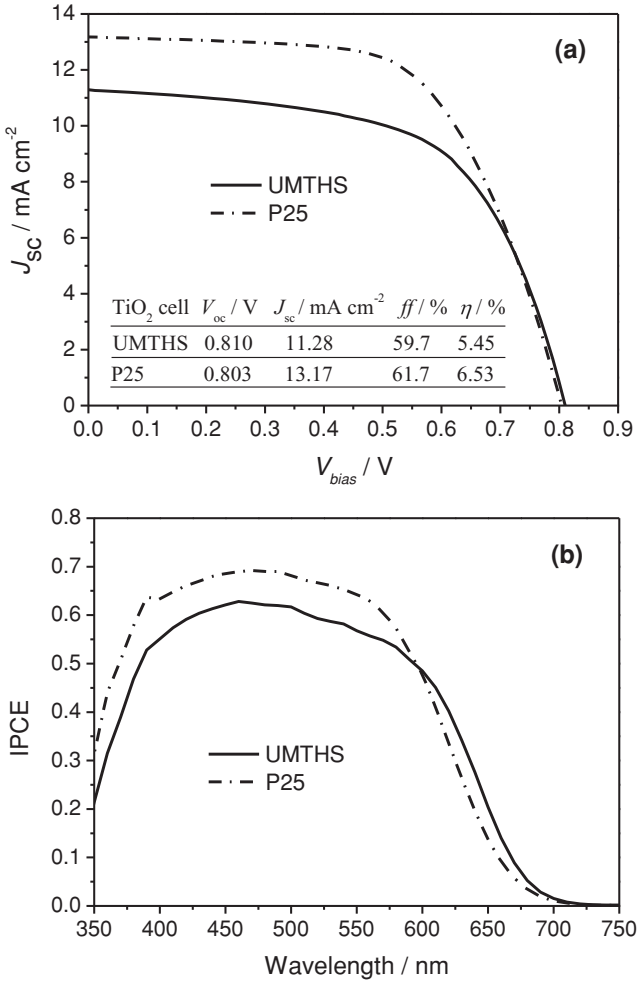

TiO_2 cell	V_{oc} / V	J_{sc} / mA cm^{-2}	ff / %	η / %
UMTHS	0.810	11.28	59.7	5.45
P25	0.803	13.17	61.7	6.53

Figure 10. *J–V* (a) and IPCE (b) characteristics of Z907 dye-sensitized UMTHS and P25 solar cells. The inset of (a) shows their photovoltaic parameters.

carriers; and (3) 1D single-crystal anatase nanothorns facilitating the charge carrier separation.

UMTHS have been reported to be an excellent light-scattering material for DSCs to assist the light harvesting.[43,44] Considering their high surface area, here we directly utilized UMTHS to fabricate the active layer of photoanode for the Z907-sensitized TiO_2 solar cell using Pt counter electrode. As shown in **Figure 10**a, UMTHS-based solar cells using $Co(bpy)_3^{3+/2+}$ electrolytes yields impressive power conversion efficiency (η) of 5.5% under AM1.5 one-sun illumination, fairly comparable to the optimized P25 cell equipped with an additional scattering layer.[45]

Figure 10b shows their incident photon-to-current conversion efficiency (IPCE) spectra. Interestingly, UMTHS photoanode without scattering layer even exhibits superior external quantum efficiency to the optimized P25 layer coupled with an additional scattering layer in the long wavelength region (λ > 600 nm). It is believed that light harvesting of the sensitized UMTHS is dramatically improved by enhanced light scattering of the hollow and hierarchical structures.[33,43] In addition, the hollow interior of UMTHS is expected to facilitate the mass transport of $Co(bpy)_3^{3+/2+}$ in the electrolyte,[46] which is one of the limiting factors for cobalt complex based electrolytes. Based on these preliminary results, it is envisioned that there is ample space to further improve the photovoltaic performance of UMTHS-based photoanodes by taking advantages of their hollow and hierarchical structures. Further studies are currently in progress in our group to optimize UMTHS-based photoanodes for the high-efficiency dye-sensitized mesoscopic solar cells.

3. Conclusions

We have demonstrated a targeted etching strategy for the controllable synthesis of UMTHS from the hydrothermal treatment of amorphous hydrous F-TiO_2 solid spheres with the PVP coating. With the penetration of water, the assembled hydrates are gradually crystallized to anatase with a preferential grow along (101) plane, while the inner core is selectively etched and hollowed by the adsorbed F^-, eventually forming robust hollow spheres with numerous radially arranged single-crystal anatase nanothorns

on the shell. This approach is green, remarkably effective, reproducible and scalable, with which gram-scale porous TiO_2 hollow spheres with tunable particle size and interior structures could be prepared by using the most economic amount of fluoride. More notably, this synthetic method delivers the largest-scale synthesis of TiO_2 hollow spheres amongst various template-free routes, and the resultant UMTHS have the largest surface area up to 128.6 m^2 g^{-1} among the hierarchical TiO_2 spheres with well-defined crystal facets reported up to now.[14,26,48] This strategy has also proved the feasibility of chemical reconstruction of hydrous TiO_2 spheres to mesoporous anatase spheres with tunable inner structures ranging from the conventional solid spheres[7,11,33,35] to hollow and complex core-shell and yolk-shell structures if one rationally chooses proper AHTSS and etching process. The synthesized TiO_2 hollow spheres present excellent performances for photocatalytic removal of NO_x and DSCs, compared with the commercially available Aeroxide TiO_2 P25. It is anticipated that this facile synthetic strategy can be applied to produce other semiconducting metal oxides for advanced energy, environmental and other related applications.

4. Experimental Section

Synthesis of AHTSS: In a typical synthesis of AHTSS with a uniform particle size ca. 490 nm synthesized at a R_H value of 5, $NH_3{\cdot}H_2O$ (28%, 0.38 g) solution and H_2O (0.91 g) were added into a mixed solution (250 ml) containing ethanol and acetonitrile (6:4 in volume ratio). Then $Ti(O\text{-}iPr)_4$ (5 mL) was promptly injected into the above solution under vigorous stirring. A milky suspension was formed in 2 s. After continuous stirring for 6 h, the formed AHTSS were centrifuged and washed with ethanol for 2 times in order to remove the unreacted precursors. Finally the samples were washed with water for 2 times.

Synthesis of UMTHS: Typically, dried AHTSS (1.5 g) were re-dispersed in water (30 mL). Fluorides, NaF, KF, or NH_4F were then added into the suspension as the etching agents. The molar ration for F/Ti (R_F) was controlled to 0.12, taking account of the final weight percentage of TiO_2 in AHTSS. Without specially mentioned, NaF (0.13 g) was used. After stirring for 1 h, PVP (0.15 g) with an average molecular weight (AMW) of 10 K was added. The suspension was stirred for another 1 h before transferred to a Teflon-lined autoclave (45 mL). A hydrothermal reaction was carried out at 110 °C for 4 h to conduct the crystallization and targeted etching processes. The obtained white UMTHS were collected. After washing with diluted NaOH solution (1 mmol L^{-1}) and water, the final UMTHS were obtained by calcining at 350 °C for 2 h with a ramping rate of 1 °C min^{-1}. For comparison, mesoporous TiO_2 solid spheres (MTSS) were also prepared at a R_F value of 0.08.

Synthesis of UMTHS with Core–Shell and Yolk–Shell Structures: AHTSS (1.5 g) were re-dispersed in water (30 mL). PEG (AMW: 1 K; 0.1 g) was added into the solution. The solution was stirred and ultrasonicated to fill PEG into the pores of AHTSS. Then the product was mixed with NaF (0.1 g). After stirring for 1 h, PVP (0.15 g) was added. The resulting suspension was stirred for another 1 h before transferred to a Teflon-lined autoclave (45 mL). A hydrothermal reaction was carried out at 110 °C for 3 h to fully crystallize the TiO_2 species. The white products were collected and washed with diluted NaOH solution (10 mmol L^{-1}) and water. Finally, the samples were calcined at 350 °C for 3 h with a ramping rate of 1 °C min^{-1}.

Materials Characterization: XRD patterns were obtained by using a Bruker D8 Advance X-ray diffractometer with a monochromated high-intensity Cu K radiation of wavelength $\lambda = 0.15418$ nm. The morphology and microstructure were characterized by a Zeiss Supra 40 field-effect scanning electron microscope and a transmission electron microscope (TEM, JEOL JEM-2010). Nitrogen adsorption-desorption isotherms were obtained at liquid nitrogen temperature (77 K) measured by an ASAP 2020 system (Micromeritics). Before measurement, all the crystallized TiO_2 samples (0.1–0.2 g), UMTHS and MTSS, were outgassed under vacuum for 6 h at 200 °C. While for AHTSS, the conditions were set to 12 h at 100 °C. The Brunauer-Emmett-Teller (BET) equation was used to calculate the surface area from adsorption data obtained at $P/P_0 = 0.01–0.30$. The average pore diameter was estimated using the Barrett-Joyner-Halenda (BJH) method from the adsorption branch of the isotherm. Thermogravimetric analysis (TGA) was performed using a TA Instruments TGA 2950 high-resolution thermogravimetric analyzer with a DuPont 2100 thermal analyst controller. The TGA was carried out in air with a heating rate of 10 °C min^{-1}.

Photocatalytic NO Oxidation: The photocatalytic oxidation of NO-containing continuous gas flow over TiO_2 was accomplished according to ISO 22197-1: 2007. Before measurement, TiO_2 samples were exposed to UV illumination for 72 h to eliminate residual organic contaminants on the surface. Detailed test equipment and procedures were described previously.[41,42] The inlet concentration of NO in air was adjusted to 1 ppm, and the relative humidity was adjusted to 50%. The gas was passed by TiO_2 that was preloaded in a holder with a surface area of 9 cm^2. Under a UV(A) irradiation by a light source (Philips, Cleo Compact, $\lambda_{max} = 355$ nm, 15 W) with a light intensity of 1 mW cm^{-2}, the gaseous concentrations of NO, NO_2, and the sum of them, NO_x were detected by a pollutant analyzer (NO_x-Analyser, Horiba, APNA 360).

The photonic efficiency ζ (mol $einstein^{-1}$) was calculated as a ratio of the number changes of NO, NO_2 and NO_x gas molecules ($n_{molecules}$) to the number of incident photons (n_{photos}) during the illumination period:

$$\zeta = \frac{n_{molecules}}{n_{photos}} = \frac{\int_{t_0}^{t_1} AX\,dt}{I\,(t_1 - t_0)} \quad (1)$$

where t_0 and t_1 are the time moments when UV light was switched on and off, respectively. A is the coefficient taken as a product of the gas flow rate value and of the value 10^{-6} expressed in mol s^{-1} ($A = 2.08 \times 10^{-9}$ mol s^{-1}). X, taken in ppm, is either the degraded concentration of NO/NO_x or the generated NO_2 concentration. I is the incident photon flux (mol s^{-1}) on certain surface area (S) of photocatalysts:

$$I = \frac{I'\lambda S}{Nhc} \quad (2)$$

where I' is the intensity of the incident light, λ is the wavelength at maximum emission of the UVA lamp used ($\lambda = 355$ nm), and, N, h, c are the Avogadro number, the Planck constant and the speed of light, correspondingly. The calculated value of I was 0.26×10^{-7} einstein s^{-1}.

Preparation and Characterization of DSCs: UMTHS were mixed with ethyl cellulose and α-terpineol following a previously reported procedure.[47–49] The formed viscous paste was repeatedly screen-printed onto FTO glass (TEC, 15 Ω sq^{-1}) and finally calcined in air at 450 °C for 15 min. The thickness of the electrodes was ~9 μm, as determined by an Alpha-Step IQ surface profiler (KLA-Tencor instruments). For comparison, photoanode using P25 as a TiO_2 source was also prepared according to a similar procedure but with an additional deposition with a 2 μm scattering layer of larger TiO_2 particles (ca. 400 nm, WER-O paste, Dyesol). Finally, the as-calcined UMTHS and P25 photoanodes were subjected to a diluted $TiCl_4$ solution, rinsed, dried and heated to 450 °C in a hot air stream for 30 min.

The obtained TiO_2 photoanodes were immersed into an acetonitrile: *tert*-butanol (1:1 in a volume ratio) solution of Z907 dye (*cis*-diisothiocyanato-(2,2′-bipyridyl-4,4′-dicarboxylic acid)-(2,2′-bipyridyl-4,4′-dinonyl) ruthenium-(II), 0.15 mmol L^{-1}) and left overnight before being removed and rinsed in acetonitrile. FTO with a thin Pt layer was used as the counter electrode. Pt was deposited on the conductive side of FTO glass by thermal decomposition of hexachloroplatinic acid at 450 °C for 30 min. $[Co(bpy)_3](PF_6)_2$ (0.2 mol L^{-1}), $[Co(bpy)_3](PF_6)_3$ (bpy = 2,2′-bipyridine) (0.02 mol L^{-1}), $LiClO_4$ (0.1 mol L^{-1}), and 4-*tert*-butylpyridine (0.5 mol L^{-1}) in acetonitrile was used as cobalt complex electrolyte. Detailed synthetic procedure for cobalt complex electrolyte can be found in our previous report.[45]

Current–voltage characteristics under simulated AM 1.5 illumination were measured using a Keithley Source Meter and the PVIV software package (Newport). Simulated AM 1.5 illumination was provided by a Newport solar simulator, and light intensity was measured using a calibrated Si solar cell. The active area of the cells was defined by a mask to be 0.1199 cm^2. IPCE spectra were measured with a spectral resolution of 5 nm, using a 300 W xenon lamp and a grating monochromator equipped with order sorting filters (Newport/Oriel). The incident photon flux was determined by using a calibrated silicon photodiode (Newport/Oriel). Photocurrents were measured with an auto-ranging current amplifier (Newport/Oriel). Control of the monochromator and recording of the photocurrent spectra were performed with a PC running the TRACQ Basic software (Newport).

Supporting Information

Supporting Information is available from the Wiley Online Library or from the author.

Acknowledgements

This work was financially supported by URC Grant No. R-284-000-075-112, and NRF CRP Grant No. R-284-000-079-592. We acknowlege the early work conducted by Mr. Wee Chong Tan. Dr. J. H. Pan is grateful to the Alexander von Humboldt (AvH) Foundation for granting him a research fellowship. Figure 10a was corrected and Reference 40 was updated on August 23, 2013.

Received: March 15, 2013
Revised: June 6, 2013
Published online: August 21, 2013

[1] Y. Tachibana, L. Vayssieres, J. R. Durrant, *Nat. Photonics* **2012**, *6*, 511–518.
[2] A. Kubacka, M. Fernández-García, G. Colón, *Chem. Rev.* **2011**, *112*, 1555–1614.
[3] J. Hu, M. Chen, X. Fang, L. Wu, *Chem. Soc. Rev.* **2011**, *40*, 5472–5491.
[4] X. W. Lou, L. A. Archer, Z. Yang, *Adv. Mater.* **2008**, *20*, 3987–4019.
[5] K. An, T. Hyeon, *Nano Today* **2009**, *4*, 359–373.
[6] M. R. Hoffmann, S. T. Martin, W. Choi, D. W. Bahnemann, *Chem. Rev.* **1995**, *95*, 69–96.
[7] F. Huang, D. Chen, X. L. Zhang, R. A. Caruso, Y. B. Cheng, *Adv. Funct. Mater.* **2010**, *20*, 1301–1305.
[8] J. H. Pan, H. Dou, Z. Xiong, C. Xu, J. Ma, X. S. Zhao, *J. Mater. Chem.* **2010**, *20*, 4512–4528.
[9] A. A. Ismail, D. W. Bahnemann, *J. Mater. Chem.* **2011**, *21*, 11686–11707.
[10] Z. Sun, J. H. Kim, Y. Zhao, F. Bijarbooneh, V. Malgras, Y. Lee, Y.-M. Kang, S. X. Dou, *J. Am. Chem. Soc.* **2011**, *133*, 19314–19317.
[11] D. Chen, R. A. Caruso, *Adv. Funct. Mater.* **2013**, *23*, 1356–1374.
[12] Z. Wang, L. Zhou, X. W. Lou, *Adv. Mater.* **2012**, *24*, 1903–1911.
[13] Y. Zhao, L. Jiang, *Adv. Mater.* **2009**, *21*, 3621–3638.
[14] D. Wu, F. Zhu, J. Li, H. Dong, Q. Li, K. Jiang, D. Xu, *J. Mater. Chem.* **2012**, *22*, 11665–11671.
[15] S. Liu, J. Yu, B. Cheng, M. Jaroniec, *Adv. Colloid Interface Sci.* **2012**, *173*, 35–53.
[16] W. Li, Y. Deng, Z. Wu, X. Qian, J. Yang, Y. Wang, D. Gu, F. Zhang, B. Tu, D. Zhao, *J. Am. Chem. Soc.* **2011**, *133*, 15830–15833.
[17] T. Leshuk, S. Linley, G. Baxter, F. Gu, *ACS Appl. Mater. Interfaces* **2012**, *4*, 6062–6070.
[18] J. B. Joo, Q. Zhang, I. Lee, M. Dahl, F. Zaera, Y. Yin, *Adv. Funct. Mater.* **2012**, *22*, 166–174.
[19] K. Lv, B. Cheng, J. Yu, G. Liu, *PCCP* **2012**, *14*, 5349–5362.
[20] H. C. Zeng, *J. Mater. Chem.* **2011**, *21*, 7511–7526.
[21] J. G. Yu, Y. R. Su, B. Cheng, *Adv. Funct. Mater.* **2007**, *17*, 1984–1990.
[22] H. Li, Z. Bian, J. Zhu, D. Zhang, G. Li, Y. Huo, H. Li, Y. Lu, *J. Am. Chem. Soc.* **2007**, *129*, 8406–8407.
[23] J. H. Pan, X. Zhang, A. J. Du, D. D. Sun, J. O. Leckie, *J. Am. Chem. Soc.* **2008**, *130*, 11256–11257.
[24] H. G. Yang, H. C. Zeng, *J. Phys. Chem. B* **2004**, *108*, 3492–3495.
[25] J. Li, H. C. Zeng, *J. Am. Chem. Soc.* **2007**, *129*, 15839–15847.
[26] S. Liu, J. Yu, M. Jaroniec, *J. Am. Chem. Soc.* **2010**, *132*, 11914–11916.
[27] J. Yu, J. Zhang, *Dalton Trans.* **2010**, *39*, 5860–5867.
[28] Q. Zhang, T. Zhang, J. Ge, Y. Yin, *Nano Lett.* **2008**, *8*, 2867–2871.
[29] Y. Chen, H. Chen, L. Guo, Q. He, F. Chen, J. Zhou, J. Feng, J. Shi, *ACS Nano* **2009**, *4*, 529–539.
[30] Q. Yu, P. Wang, S. Hu, J. Hui, J. Zhuang, X. Wang, *Langmuir* **2011**, *27*, 7185–7191.
[31] T. Sugimoto, T. Kojima, *J. Phys. Chem. C* **2008**, *112*, 18760–18771.
[32] Q. Zhang, I. Lee, J. Ge, F. Zaera, Y. Yin, *Adv. Funct. Mater.* **2010**, *20*, 2201–2214.
[33] D. Chen, F. Huang, Y. B. Cheng, R. A. Caruso, *Adv. Mater.* **2009**, *21*, 2206–2210.
[34] D. Chen, L. Cao, F. Huang, P. Imperia, Y.-B. Cheng, R. A. Caruso, *J. Am. Chem. Soc.* **2010**, *132*, 4438–4444.
[35] Y. J. Kim, M. H. Lee, H. J. Kim, G. Lim, Y. S. Choi, N.-G. Park, K. Kim, W. I. Lee, *Adv. Mater.* **2009**, *21*, 3668–3673.
[36] D. Wang, L. Liu, F. Zhang, K. Tao, E. Pippel, K. Domen, *Nano Lett.* **2011**, *11*, 3649–3655.
[37] J. H. Pan, Z. Cai, Y. Yu, X. S. Zhao, *J. Mater. Chem.* **2011**, *21*, 11430–11438.
[38] S. Eiden-Assmann, J. Widoniak, G. Maret, *Chem. Mater.* **2003**, *16*, 6–11.
[39] Y. Hu, J. Ge, Y. Sun, T. Zhang, Y. Yin, *Nano Lett.* **2007**, *7*, 1832–1836.
[40] J. H. Pan, Q. Wang, D. W. Bahnemann, *Catal. Today* **2013**, DOI: 10.1016/j.cattod.2013.08.007.
[41] R. Dillert, J. Stötzner, A. Engel, D. W. Bahnemann, *J. Hazard. Mater.* **2012**, 211–212, 240–246.
[42] A. Mitsionis, T. Vaimakis, C. Trapalis, N. Todorova, D. Bahnemann, R. Dillert, *Appl. Catal. B: Environ.* **2011**, *106*, 398–404.
[43] H. J. Koo, Y. J. Kim, Y. H. Lee, W. I. Lee, K. Kim, N. G. Park, *Adv. Mater.* **2008**, *20*, 195–199.
[44] H. Wang, M. Miyauchi, Y. Ishikawa, A. Pyatenko, N. Koshizaki, Y. Li, L. Li, X. Li, Y. Bando, D. Golberg, *J. Am. Chem. Soc.* **2011**, *133*, 19102–19109.
[45] Y. Liu, J. R. Jennings, Y. Huang, Q. Wang, S. M. Zakeeruddin, M. Grätzel, *J. Phys. Chem. C* **2011**, *115*, 18847–18855.
[46] H.-S. Kim, S.-B. Ko, I.-H. Jang, N.-G. Park, *Chem. Commun.* **2011**, *47*, 12637–12639.
[47] S. Ito, T. N. Murakami, P. Comte, P. Liska, C. Grätzel, M. K. Nazeeruddin, M. Grätzel, *Thin Solid Films* **2008**, *516*, 4613–4619.
[48] M. A. Hossain, J. R. Jennings, C. Shen, J. H. Pan, Z. Y. Koh, N. Mathews, Q. Wang, *J. Mater. Chem.* **2012**, *22*, 16235–16242.
[49] M. A. Hossain, J. R. Jennings, Z. Y. Koh, Q. Wang, *ACS Nano* **2011**, *5*, 3172–3181.